

# Constraints on primordial non-Gaussianity from *Planck* PR4 data

Gabriel Jung<sup>1</sup>, Michele Citran<sup>2,3</sup>, Bartjan van Tent<sup>2</sup>, Léa Dumilly<sup>1</sup>, and Nabila Aghanim<sup>1</sup>

<sup>1</sup> Université Paris-Saclay, CNRS, Institut d’Astrophysique Spatiale, 91405 Orsay, France

<sup>2</sup> Université Paris-Saclay, CNRS/IN2P3, IJCLab, 91405 Orsay, France

<sup>3</sup> Université Paris Cité, CNRS, Astroparticule et Cosmologie, 75013 Paris, France

## ABSTRACT

We perform the first bispectrum analysis of the final *Planck* release temperature and E-polarization CMB data, called PR4. We use the binned bispectrum estimator pipeline that was also used for the previous *Planck* releases as well as the integrated bispectrum estimator. We test the standard primordial (local, equilateral and orthogonal) and secondary (lensing, unclustered point sources and CIB) bispectrum shapes. The final primordial results of the full T+E analysis are  $f_{\text{NL}}^{\text{local}} = -0.1 \pm 5.0$ ,  $f_{\text{NL}}^{\text{equil}} = 6 \pm 46$  and  $f_{\text{NL}}^{\text{ortho}} = -8 \pm 21$ . These results are consistent with previous *Planck* releases, but have slightly smaller error bars than in PR3, up to 12% smaller for orthogonal. They represent the best *Planck* constraints on primordial non-Gaussianity. The lensing and point source bispectra are also detected, consistent with PR3. We perform several validation tests and find in particular that the 600 simulations, used to determine the linear correction term and the error bars, have a systematically low lensing bispectrum. We show however that this has no impact on our results.

## 1. Introduction

Primordial non-Gaussianity (PNG) is the field of study of deviations from Gaussianity of the primordial cosmological fluctuations. A wealth of information is expected to be encoded into the non-Gaussianity of the fluctuations, in particular regarding the period of the production of these fluctuations, most generally expected to be a model of inflation (see e.g. the reviews Bartolo et al. 2004; Chen 2010; Wang 2014; Renaux-Petel 2015; Achúcarro et al. 2022). For example, the size (parametrized by the so-called  $f_{\text{NL}}$  parameters) and type of non-Gaussianity, once detected, will allow us to distinguish between inflation models with multiple fields (see e.g. Vernizzi & Wands 2006; Rigopoulos et al. 2007; Byrnes & Choi 2010; Jung & van Tent 2017; de Putter et al. 2017; Wang et al. 2023), models with non-standard kinetic terms (see e.g. Seery & Lidsey 2005; Chen et al. 2007; Bartolo et al. 2010), or the standard single-field slow-roll models of inflation (Maldacena 2003). PNG can also put constraints on other models of the early universe than inflation, see e.g. Lehnert (2010); Agullo et al. (2018); van Tent et al. (2023). Together with the tensor-to-scalar ratio, PNG is the main primordial observable that we hope to measure in the future. The tensor-to-scalar ratio will tell us the energy scale at which inflation happened and, together with the already observed amplitude and spectral index (slope) of the scalar power spectrum, allow us to determine also the first and second derivatives of the inflaton potential at that scale, at least for single-field slow-roll models (see e.g. Baumann 2011, for a review of inflation theory). However, as indicated above, non-Gaussianity contains much more information for distinguishing between inflation models and, contrary to the tensor-to-scalar ratio which could be arbitrarily small and hence unobservable, it has an explicit lower limit that is the prediction of single-field slow-roll inflation (Maldacena 2003) (although that limit is about two orders of magnitude smaller than what we can hope to measure with the CMB alone). In addition, PNG could show the presence of new massive particles in the context of the so-called cosmological collider (Arkani-Hamed & Maldacena 2015).

It is hence no wonder that PNG was an important focus of cosmological surveys, mainly the cosmic microwave background (CMB) satellite missions of the past, *WMAP* (see e.g. Komatsu et al. 2011; Bennett et al. 2013) and *Planck*, and remains so for future missions like *LiteBIRD* (Allys et al. 2023) (see also e.g. Finelli et al. 2018). In particular, the *Planck* collaboration dedicated a full paper to PNG at each of its three official releases (PR1, PR2, and PR3), Planck Collaboration (2014, 2016, 2020d). The third of these has the most stringent observational constraints to date on a large number of types of non-Gaussianity. A similar level of constraints should in principle be reached or even improved upon with the new generation of galaxy surveys like *Euclid* (Euclid Collaboration 2011), see e.g. Karagiannis et al. (2018), but currently they are not yet competitive with the CMB results (see D’Amico et al. 2022; Cabass et al. 2022b,a; Ivanov et al. 2024; Cagliari et al. 2025, for constraints based on the *BOSS* data). To determine the CMB bispectrum (the Fourier or spherical harmonic transform of the three-point correlator), which is the object where one generically expects the strongest PNG signal and the exclusive focus of this paper, three main estimators were used in the *Planck* papers: the KSW estimator (Komatsu et al. 2005; Yadav et al. 2007, 2008), the binned estimator (Bucher et al. 2010, 2016), and the modal estimator (Fergusson et al. 2010, 2012; Fergusson 2014).

After the third *Planck* release, a part of the collaboration continued to work on the data-processing pipeline, creating a new one called NPIPE, which led to a final release, PR4 (Planck Collaboration 2020e). However, this release of data products was not accompanied by the usual suite of analysis papers. The cosmological parameters determined from the power spectra of PR4 were finally published in Tristram et al. (2024). However, no non-Gaussian analysis had been performed on the PR4 data so far.<sup>1</sup> In addition to including previously neglected data from the repointing periods, NPIPE processed all the *Planck* channels within the same framework, including the latest versions of cor-

<sup>1</sup> While finalizing this work, a paper appeared on the arXiv using the PR4 data to study the trispectrum (four-point correlator): Philcox (2025).

rections for systematics and data treatment. This means lower noise levels and fewer systematics in PR4 compared to PR3.

In this work we perform the first bispectrum analysis of the PR4 data. We use both the effectively optimal (meaning optimal given the error bars) binned bispectrum estimator that was also used for all previous *Planck* releases, and an additional estimator that was developed later: the integrated bispectrum estimator (Jung et al. 2020). The integrated bispectrum estimator is non-optimal and has only been developed for temperature, but it is very fast and allows us to cross-check results and do additional tests. We analyze the standard primordial (local, equilateral and orthogonal) and secondary (lensing, unclustered point sources and CIB) bispectrum shapes. We perform various validation tests and in particular look very carefully at the 600 CMB and noise simulations that are used both for the linear correction term and for the error bars.

The outline of the paper is as follows. In section 2 we define the CMB bispectrum and in particular its binned and integrated approximations. In section 3 we recall the theoretical templates we will test for and the expression of the  $f_{\text{NL}}$  estimators. In section 4 we describe the data and simulations we use. The main results of our paper are given in section 5, followed by section 6 with validation tests to confirm their robustness. We conclude in section 7.

## 2. The CMB bispectrum

### 2.1. Definitions

To study small deviations from Gaussianity in the CMB, a key observable is the angle-averaged bispectrum defined by

$$B_{\ell_1 \ell_2 \ell_3}^{p_1 p_2 p_3} \equiv \left\langle \int_{S^2} d\hat{\Omega} M_{\ell_1}^{p_1}(\hat{\Omega}) M_{\ell_2}^{p_2}(\hat{\Omega}) M_{\ell_3}^{p_3}(\hat{\Omega}) \right\rangle, \quad (1)$$

where maps of the CMB temperature or E-polarization field denoted by the label  $p$  are filtered using the standard decomposition into spherical harmonics:

$$M_{\ell}^p(\hat{\Omega}) = \sum_{m=-\ell}^{+\ell} a_{\ell m}^p Y_{\ell m}(\hat{\Omega}). \quad (2)$$

One can show that this angle-averaged bispectrum is related to the full angular bispectrum, which is defined as the three-point correlator of the harmonic coefficients, under the assumption of statistical isotropy by

$$B_{\ell_1 \ell_2 \ell_3} = h_{\ell_1 \ell_2 \ell_3} \sum_{m_1, m_2, m_3} \begin{pmatrix} \ell_1 & \ell_2 & \ell_3 \\ m_1 & m_2 & m_3 \end{pmatrix} \langle a_{\ell_1 m_1} a_{\ell_2 m_2} a_{\ell_3 m_3} \rangle, \quad (3)$$

where

$$h_{\ell_1 \ell_2 \ell_3} = \sqrt{\frac{(2\ell_1 + 1)(2\ell_2 + 1)(2\ell_3 + 1)}{4\pi}} \begin{pmatrix} \ell_1 & \ell_2 & \ell_3 \\ 0 & 0 & 0 \end{pmatrix}. \quad (4)$$

Due to the presence of the  $3j$  Wigner symbol in  $h_{\ell_1 \ell_2 \ell_3}$ , we need to consider only  $\ell$ -triplets that respect both the parity condition ( $\ell_1 + \ell_2 + \ell_3$  even) and the triangle inequality ( $|\ell_1 - \ell_2| \leq \ell_3 \leq \ell_1 + \ell_2$ ).

Assuming weak non-Gaussianity, the bispectrum covariance matrix in polarization space becomes

$$\text{Covar}(B_{\ell_1 \ell_2 \ell_3}^{p_1 p_2 p_3}, B_{\ell_1 \ell_2 \ell_3}^{p_4 p_5 p_6}) = g_{\ell_1 \ell_2 \ell_3} h_{\ell_1 \ell_2 \ell_3}^2 C_{\ell_1}^{p_1 p_4} C_{\ell_2}^{p_2 p_5} C_{\ell_3}^{p_3 p_6}, \quad (5)$$

where the factor  $g_{\ell_1 \ell_2 \ell_3}$  is 6 when the three  $\ell$ 's are the same, 2 when only two are equal and 1 otherwise.

In practice, measuring the bispectrum for all valid configurations is computationally prohibitive. To address this challenge, several approaches have been developed, including the binned bispectrum and integrated bispectrum estimators, which we discuss in the following.

### 2.2. Binned bispectrum

The binned bispectrum method simply consists of using a binning of the multipole  $\ell$  space to drastically reduce the number of mode triplets. It is well adapted to work with relatively smooth functions in harmonic space, which is the case of the different standard bispectrum templates we discuss later in Sect. 3.1. The binned bispectrum estimator and its implementation are described in Bucher et al. (2016) (see also Bucher et al. 2010; Jung et al. 2018, for details).

The binned bispectrum estimator can be written as

$$\hat{B}_{i_1 i_2 i_3}^{p_1 p_2 p_3} = \int_{S^2} d\hat{\Omega} M_{i_1}^{p_1}(\hat{\Omega}) M_{i_2}^{p_2}(\hat{\Omega}) M_{i_3}^{p_3}(\hat{\Omega}) - B_{i_1 i_2 i_3}^{p_1 p_2 p_3, \text{lin}}, \quad (6)$$

where maps filtered over the  $i$ -th bin, denoted as  $\Delta_i$ , are simply obtained using

$$M_i^p(\hat{\Omega}) = \sum_{\ell \in \Delta_i} M_{\ell}^p(\hat{\Omega}). \quad (7)$$

The linear correction term  $B_{i_1 i_2 i_3}^{p_1 p_2 p_3, \text{lin}}$  is necessary to maintain the optimality of the estimator when features breaking the expected isotropy of the signal have to be taken into account. For example with observational datasets, masking some regions of the sky like the galactic plane as well as the anisotropic scanning pattern of the mission which leads to anisotropic noise levels, have such an effect. This correction is computed using

$$B_{i_1 i_2 i_3}^{p_1 p_2 p_3, \text{lin}} = \int_{S^2} d\hat{\Omega} \left[ M_{i_1}^{p_1} \left\langle M_{i_2}^{p_2} M_{i_3}^{p_3} \right\rangle + M_{i_2}^{p_2} \left\langle M_{i_1}^{p_1} M_{i_3}^{p_3} \right\rangle + M_{i_3}^{p_3} \left\langle M_{i_1}^{p_1} M_{i_2}^{p_2} \right\rangle \right], \quad (8)$$

where the ensemble averages are calculated over CMB simulations with the same characteristics as the observations (beam, noise and mask). Moreover, the estimated binned bispectrum should be multiplied by the factor  $1/f_{\text{sky}}$ , with  $f_{\text{sky}}$  the unmasked fraction of the sky, before any comparison to full-sky theoretical predictions.

From a known theoretical bispectrum template (see Sect. 3.1 for examples), it is straightforward to compute the corresponding theoretical binned bispectrum

$$B_{i_1 i_2 i_3}^{p_1 p_2 p_3, \text{th}} = \sum_{\ell_1 \in \Delta_1} \sum_{\ell_2 \in \Delta_2} \sum_{\ell_3 \in \Delta_3} B_{\ell_1 \ell_2 \ell_3}^{p_1 p_2 p_3, \text{th}}. \quad (9)$$

The covariance matrix of the binned bispectrum in polarization space is given by

$$\begin{aligned} \text{Covar}(B_{i_1 i_2 i_3}^{p_1 p_2 p_3}, B_{i_1 i_2 i_3}^{p_4 p_5 p_6}) &\equiv V_{i_1 i_2 i_3}^{p_1 p_2 p_3 p_4 p_5 p_6} \\ &= g_{i_1 i_2 i_3} \\ &\times \sum_{\ell_1 \in \Delta_1} \sum_{\ell_2 \in \Delta_2} \sum_{\ell_3 \in \Delta_3} h_{\ell_1 \ell_2 \ell_3}^2 C_{\ell_1}^{p_1 p_4} C_{\ell_2}^{p_2 p_5} C_{\ell_3}^{p_3 p_6}. \end{aligned} \quad (10)$$

To take into account instrumental effects, one has to apply the following modifications to Eqs. (9) and (10)

$$C_{\ell} \rightarrow b_{\ell}^2 C_{\ell} + N_{\ell}, \quad B_{\ell_1 \ell_2 \ell_3} \rightarrow b_{\ell_1} b_{\ell_2} b_{\ell_3} B_{\ell_1 \ell_2 \ell_3}, \quad (11)$$

where  $b_{\ell}$  is the beam window function and  $N_{\ell}$  the noise power spectrum.

### 2.3. Integrated bispectrum

The integrated bispectrum method follows a different and simpler approach to extract the relevant bispectral information. Based on the original idea of Chiang et al. (2014), developed in the context of large-scale structure study, it consists of dividing the sky into many equal-size patches and computing the average correlation of the mean value and the power spectrum in each patch. We adopt the same methodology as in Jung et al. (2020), recalling here only the key steps.

The full integrated bispectrum estimator can be written as

$$\hat{\mathbf{B}}_\ell = \frac{1}{N_{\text{patch}}} \sum_{\text{patch}} \overline{M}^{\text{patch}} C_\ell^{\text{patch}} - \mathbf{B}_\ell^{\text{lin}}, \quad (12)$$

where  $\overline{M}^{\text{patch}}$  and  $C_\ell^{\text{patch}}$  are respectively the measured mean value and power spectrum in a given patch, and  $N_{\text{patch}}$  is the total number of patches. Note that in this expression, we drop the  $p$  subscript, as we only consider temperature maps with the integrated bispectrum estimator in this work. Similarly to the binned bispectrum case, the linear correction term  $\mathbf{B}_\ell^{\text{lin}}$  is used to maintain optimality when anisotropy breaking effects (mask, anisotropic noise) are present in the data. It takes the form

$$\mathbf{B}_\ell^{\text{lin}} = \frac{1}{N_{\text{patch}}} \sum_{\text{patch}} \overline{M}^{\text{patch}} C_\ell^{\text{patch,sims}}, \quad (13)$$

where the  $C_\ell^{\text{patch,sims}}$  are evaluated from a sufficiently large set of simulations reproducing the main characteristics of observations (e.g., mask, noise and beam). Additionally, the estimated integrated bispectrum is multiplied by the factor  $1/f_{\text{sky}}$  if the sky is partially masked.

One can directly relate the theoretical expectation of the integrated bispectrum and the theoretical bispectrum template, and the expression only depends on the shape, size, and position of the patches. In the case of azimuthally symmetric patches, this link is given by:

$$\mathbf{B}_\ell^{\text{th}} = \frac{1}{(4\pi)^3} \sum_{\ell_1 \ell_2 \ell_3 \ell_4 \ell_5} w_{\ell_3} w_{\ell_4} w_{\ell_5} \mathcal{F}_{\ell \ell_1 \ell_2 \ell_3 \ell_4 \ell_5} \mathbf{B}_{\ell_1 \ell_2 \ell_3}^{\text{th}}, \quad (14)$$

where the factor

$$\begin{aligned} \mathcal{F}_{\ell \ell_1 \ell_2 \ell_3 \ell_4 \ell_5} &\equiv (-1)^{\ell_2 + \ell_4} (2\ell_4 + 1)(2\ell_5 + 1) \begin{pmatrix} \ell_1 & \ell_2 & \ell_3 \\ 0 & 0 & 0 \end{pmatrix}^{-1} \\ &\times \begin{pmatrix} \ell & \ell_1 & \ell_4 \\ 0 & 0 & 0 \end{pmatrix} \begin{pmatrix} \ell & \ell_2 & \ell_5 \\ 0 & 0 & 0 \end{pmatrix} \begin{pmatrix} \ell_3 & \ell_4 & \ell_5 \\ 0 & 0 & 0 \end{pmatrix} \begin{Bmatrix} \ell_1 & \ell_2 & \ell_3 \\ \ell_5 & \ell_4 & \ell \end{Bmatrix} \end{aligned} \quad (15)$$

only depends on Wigner  $3j$  and  $6j$  symbols (in parentheses and braces, respectively), and  $w_\ell$  is a simple function in harmonic space that defines the full set of patches.<sup>2</sup> In this work, we use the same set of patches as in Jung et al. (2020) defined by  $w_\ell = 1$  for  $\ell \leq 10$  and 0 otherwise. This implies that we probe only the squeezed limit of the bispectrum.

<sup>2</sup> The real-space map of a chosen azimuthally symmetric patch centered at  $\hat{\Omega}^{\text{patch}}$  is given by  $W(\hat{\Omega}, \hat{\Omega}^{\text{patch}}) = \sum_\ell w_\ell \frac{2\ell+1}{4\pi} P_\ell(\hat{\Omega} \cdot \hat{\Omega}^{\text{patch}})$  where  $P_\ell$  is a Legendre polynomial.

The covariance of the integrated bispectrum can be computed in a similar manner using the weakly non-Gaussian approximation and Eq. (5):

$$\begin{aligned} \text{IC}_{\ell\ell'} &\equiv \text{Covar}(\mathbf{B}_\ell, \mathbf{B}_{\ell'}) \\ &= \frac{1}{(4\pi)^6} \sum_{\ell_1 \ell_2 \ell_3 \ell_4 \ell_5 \ell'_4 \ell'_5} h_{\ell_1 \ell_2 \ell_3}^2 \mathcal{F}_{\ell \ell_1 \ell_2 \ell_3 \ell_4 \ell_5} w_{\ell_3} w_{\ell_4} w_{\ell_5} w_{\ell'_4} w_{\ell'_5} C_{\ell_1} C_{\ell_2} C_{\ell_3} \\ &\times \left[ w_{\ell_3} (\mathcal{F}_{\ell' \ell_1 \ell_2 \ell_3 \ell'_4 \ell'_5} + \mathcal{F}_{\ell' \ell_2 \ell_1 \ell_3 \ell'_4 \ell'_5}) \right. \\ &+ w_{\ell_2} (\mathcal{F}_{\ell' \ell_1 \ell_3 \ell_2 \ell'_4 \ell'_5} + \mathcal{F}_{\ell' \ell_3 \ell_1 \ell_2 \ell'_4 \ell'_5}) \\ &\left. + w_{\ell_1} (\mathcal{F}_{\ell' \ell_3 \ell_2 \ell_1 \ell'_4 \ell'_5} + \mathcal{F}_{\ell' \ell_2 \ell_3 \ell_1 \ell'_4 \ell'_5}) \right]. \end{aligned} \quad (16)$$

In the realistic case, the same modifications as for the binned bispectrum (Eq. 11) should be applied to Eqs. (14) and (16).

## 3. Parametric estimation

### 3.1. Theoretical shapes

The presence of a small amount of PNG is a prediction of many different inflationary models beyond the standard single-field slow-roll scenario. These models produce distinct bispectrum shapes depending on their specific characteristics. Here, we focus on the local, equilateral, and orthogonal templates that were studied in detail in the *Planck* PNG analyses (Planck Collaboration 2014, 2016, 2020d).

These three bispectrum shapes can be written as functions of the primordial power spectrum of the gravitational potential  $P(k) = A(k/k_0)^{n_s-4}$ , where  $A$  is its amplitude,  $k_0$  the pivot scale and  $n_s$  the spectral index,

$$\begin{aligned} \mathbf{B}^{\text{local}}(k_1, k_2, k_3) &= 2[P(k_1)P(k_2) + P(k_1)P(k_3) + P(k_2)P(k_3)], \\ \mathbf{B}^{\text{equil}}(k_1, k_2, k_3) &= -6[P(k_1)P(k_2) + (2 \text{ perms})] \\ &\quad - 12 P^{2/3}(k_1)P^{2/3}(k_2)P^{2/3}(k_3) \\ &\quad + 6[P(k_1)P^{2/3}(k_2)P^{1/3}(k_3) + (5 \text{ perms})], \\ \mathbf{B}^{\text{ortho}}(k_1, k_2, k_3) &= -18[P(k_1)P(k_2) + (2 \text{ perms})] \\ &\quad - 48 P^{2/3}(k_1)P^{2/3}(k_2)P^{2/3}(k_3) \\ &\quad + 18[P(k_1)P^{2/3}(k_2)P^{1/3}(k_3) + (5 \text{ perms})]. \end{aligned} \quad (17)$$

The local type of PNG (Gangui et al. 1994) is mostly related to multiple-field inflation, where curvature perturbations can evolve on superhorizon scales (see e.g. Rigopoulos et al. 2007; Byrnes & Choi 2010). The equilateral and orthogonal templates cover a wide range of inflationary models that have non-standard kinetic terms or higher-derivative interactions (see e.g. Creminelli et al. 2006; Chen et al. 2007; Senatore et al. 2010).

The corresponding bispectra in the CMB anisotropies can then be computed using (Komatsu & Spergel 2001)

$$\begin{aligned} \mathbf{B}_{\ell_1 \ell_2 \ell_3}^{p_1 p_2 p_3, \text{th}} &= h_{\ell_1 \ell_2 \ell_3}^2 \left( \frac{2}{\pi} \right)^3 \int_0^\infty k_1^2 dk_1 \int_0^\infty k_2^2 dk_2 \int_0^\infty k_3^2 dk_3 \\ &\quad \left[ \Delta_{\ell_1}^{p_1}(k_1) \Delta_{\ell_2}^{p_2}(k_2) \Delta_{\ell_3}^{p_3}(k_3) B(k_1, k_2, k_3) \right. \\ &\quad \left. \times \int_0^\infty r^2 dr j_{\ell_1}(k_1 r) j_{\ell_2}(k_2 r) j_{\ell_3}(k_3 r) \right], \end{aligned} \quad (18)$$

where  $\Delta_\ell^p(k)$  are the radiation transfer functions and  $j_\ell$  are the spherical Bessel functions.

There are other sources of bispectral NG in the CMB due to the presence of different foregrounds. The contribution of the three main ones, that are observable in the *Planck* data, can be taken into account using the following templates.

First, the bispectrum due to gravitational lensing (in temperature caused by the correlation of the integrated Sachs-Wolfe (ISW) and lensing effects) (Hu 2000; Lewis et al. 2011) is

$$B_{\ell_1\ell_2\ell_3}^{p_1p_2p_3,\text{lens}} = h_{\ell_1\ell_2\ell_3}^2 \left[ f_{\ell_1\ell_2\ell_3}^{p_1} C_{\ell_2}^{p_2\phi} C_{\ell_3}^{p_1p_3} + (5 \text{ perms}) \right], \quad (19)$$

where the  $C_{\ell}^{p_1p_2}$ 's are lensed power spectra and  $C_{\ell}^{T\phi}$  ( $C_{\ell}^{E\phi}$ ) is the temperature(polarization)-lensing cross-power spectrum. The  $f_{\ell_1\ell_2\ell_3}^p$  factors are given by

$$\begin{aligned} f_{\ell_1\ell_2\ell_3}^T &= \frac{1}{2} [\ell_2(\ell_2 + 1) + \ell_3(\ell_3 + 1) - \ell_1(\ell_1 + 1)], \\ f_{\ell_1\ell_2\ell_3}^E &= \frac{1}{2} [\ell_2(\ell_2 + 1) + \ell_3(\ell_3 + 1) - \ell_1(\ell_1 + 1)] \\ &\quad \times \begin{pmatrix} \ell_1 & \ell_2 & \ell_3 \\ 2 & 0 & -2 \end{pmatrix} \begin{pmatrix} \ell_1 & \ell_2 & \ell_3 \\ 0 & 0 & 0 \end{pmatrix}^{-1}. \end{aligned} \quad (20)$$

The unclustered point sources NG can be described by the simple shape (Komatsu & Spergel 2001)

$$B_{\ell_1\ell_2\ell_3}^{\text{ps}} = h_{\ell_1\ell_2\ell_3}^2, \quad (21)$$

while the cosmic infrared background (CIB) contribution is given by the heuristic template (Lacasa et al. 2014; Pénin et al. 2014)

$$B_{\ell_1\ell_2\ell_3}^{\text{CIB}} = h_{\ell_1\ell_2\ell_3}^2 \left[ \frac{(1 + \ell_1/\ell_{\text{break}})(1 + \ell_2/\ell_{\text{break}})(1 + \ell_3/\ell_{\text{break}})}{(1 + \ell_0/\ell_{\text{break}})^3} \right]^q, \quad (22)$$

where the break and pivot scales are  $\ell_{\text{break}} = 70$  and  $\ell_0 = 320$ , respectively, and the index is  $q = 0.85$ .

### 3.2. Estimator

The optimal estimator of the amplitude parameter  $f_{\text{NL}}$  for a given bispectrum shape  $B^{\text{th}}$  determined from the observed bispectrum  $\hat{B}$  is

$$\hat{f}_{\text{NL}} = \frac{\langle \hat{B}, B^{\text{th}} \rangle}{\langle B^{\text{th}}, B^{\text{th}} \rangle}, \quad (23)$$

where the exact definition of the inner product denoted as  $\langle x, y \rangle$  depends on the bispectrum estimator used. For the binned and integrated bispectra, respectively, it is

$$\begin{aligned} \langle B^a, B^b \rangle^{\text{binned}} &\equiv \sum_{i_1 \leq i_2 \leq i_3} \sum_{\substack{p_1 p_2 p_3 \\ p_4 p_5 p_6}} B_{i_1 i_2 i_3}^{p_1 p_2 p_3, a} (V^{-1})_{i_1 i_2 i_3}^{p_1 p_2 p_3 p_4 p_5 p_6} B_{i_1 i_2 i_3}^{p_4 p_5 p_6, b}, \\ \langle B^a, B^b \rangle^{\text{integrated}} &\equiv \sum_{\ell_1 \ell_2} \mathbf{B}_{\ell_1}^a (\mathbf{IC}^{-1})_{\ell_1 \ell_2} \mathbf{B}_{\ell_2}^b. \end{aligned} \quad (24)$$

The expected variance of  $\hat{f}_{\text{NL}}$  is given by  $1/\langle B^{\text{th}}, B^{\text{th}} \rangle$ , which has to be multiplied by  $1/f_{\text{sky}}$  in the case of incomplete sky coverage.

Another important quantity is the bias  $f_{\text{NL}}^{(1),(2)}$  on the measurement of  $f_{\text{NL}}^{(1)}$  for a given shape  $B^{(1)}$  due to the presence of another bispectrum  $B^{(2)}$  of known amplitude  $f_{\text{NL}}^{(2)}$ :

$$f_{\text{NL}}^{(1),(2)} = -\frac{F_{12}}{F_{11}} f_{\text{NL}}^{(2)}, \quad (25)$$

where the Fisher matrix elements are  $F_{ab} = \langle B^a, B^b \rangle$ . This is relevant to subtract the impact of the fully known lensing bispectrum (see Eq. (19); its  $f_{\text{NL}}$  is known to be unity) on the PNG estimation.

If the amplitude of the other shape(s) is not known, the correct approach is to do a joint estimation of the different shapes of interest. In that case, the estimator defined in Eq. (23) becomes

$$\hat{f}_{\text{NL}}^a = \sum_b (F^{-1})_{ab} \langle \hat{B}, B^b \rangle. \quad (26)$$

In this case, the expected variance of  $\hat{f}_{\text{NL}}^a$  (also called Fisher error bars after taking a square root), which in the independent case can be written as  $1/F_{aa}$  as indicated above, becomes for the joint analysis  $(F^{-1})_{aa}$ .

## 4. Data and simulations

Our analyses are based on data and simulations from the latest *Planck* release (PR4) (see Planck Collaboration 2020e, for details). We use the temperature and polarization maps produced by the component separation technique SEVEM (Leach et al. 2008; Fernandez-Cobos et al. 2012), which removes the large NG contamination due to several galactic foregrounds (see e.g. Jung et al. 2018; Coulton & Spergel 2019). These maps, which have a beam size of 5 arcminutes, are available on the *Planck* Legacy Archive<sup>3</sup> (PLA). We also utilize the 600 corresponding CMB and noise simulations, which can be downloaded from the National Energy Research Scientific Computing Center<sup>4</sup> (NERSC).

We use the 2018 *Planck* common mask (Planck Collaboration 2020c), also available on the PLA, which leaves an observed fraction of the sky  $f_{\text{sky}} = 0.779$  and  $f_{\text{sky}} = 0.781$  for temperature and polarization, respectively. After applying this mask to the different maps, the same standard diffusive inpainting technique as for previous *Planck* releases (Bucher et al. 2016; Gruetjen et al. 2017) is used to remove spurious effects due to both the lack of small-scale power inside the mask and the edge discontinuity, both of which would bleed into the unmasked region of the map during the filtering process in harmonic space.

For comparison purposes, we also consider the results obtained previously in Planck Collaboration (2020d) and Jung et al. (2020) on the SEVEM maps (data and 300 simulations) from the previous release (PR3) (see Planck Collaboration 2020c, for more information). The binned bispectrum estimator uses the same binning for the PR4 analysis as was used for PR3, and the integrated bispectrum estimator uses the same set of patches.

In Fig. 1, we show the temperature and E-polarization noise power spectra determined from the SEVEM PR3 and PR4 simulations, as well as the full CMB+noise power spectra. This confirms the lower level of noise in the PR4 data on a wide range of scales, allowing for example to extract additional non-Gaussian information from small scales.

## 5. Main results

In this section, we present our analysis of bispectral non-Gaussianity in the latest *Planck* data. We update the constraints on PNG of the official *Planck* PNG analyses (Planck Collaboration 2014, 2016, 2020d) using a similar methodology. We study the temperature and E-polarization CMB maps produced

<sup>3</sup> <http://pla.esac.esa.int/pla/>

<sup>4</sup> <https://portal.nersc.gov/project/cmb/planck2020/>

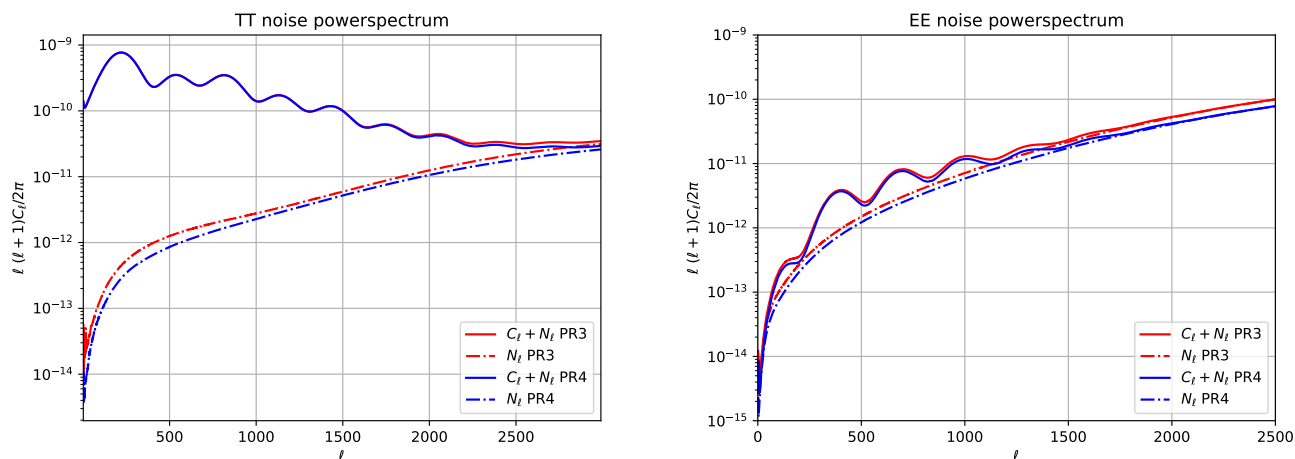


**Fig. 1.** The full and the noise-only power spectra determined from SEVEM PR3 and PR4 simulations, for temperature (left) and E-polarization (right).

by the component separation technique SEVEM for the *Planck* 2020 data release (PR4, see Sect. 4). We utilize two different bispectrum estimators to cross-validate our findings, both introduced in Sect. 2. Our main results are obtained by applying to the full dataset the binned bispectrum estimator to investigate standard shapes of primordial origin, namely the local, equilateral and orthogonal ones, and late-time NG in the form of lensing, CIB and unclustered point sources (all described in Sect. 3.1). Additionally, we use the integrated bispectrum estimator to constrain the local and lensing bispectra, which both peak in the squeezed limit, from the CMB temperature map alone.

In Table 1, we show our constraints on the PNG amplitudes  $f_{\text{NL}}^{\text{local}}$ ,  $f_{\text{NL}}^{\text{equil}}$  and  $f_{\text{NL}}^{\text{ortho}}$ . These results can be compared to Table 5 of Planck Collaboration (2020d) and Table 3 of Jung et al. (2020) for the binned and integrated bispectrum estimators, respectively. These values are obtained in independent estimations, with and without removing the bias due to the expected presence of the lensing bispectrum in the data using Eq. (25), and including scales up to  $\ell_{\text{max}} = 2500$ . The more conservative approach of analyzing jointly the lensing contribution with the PNG shapes leads to similar conclusions with only slightly larger error bars, as can be seen in Table 2. As in the analyses conducted on data from the previous *Planck* releases, the three considered  $f_{\text{NL}}$  parameters are fully compatible with zero in all cases.

Table 3 summarizes our results for the bispectrum amplitudes from late-time NG, to be compared to Tables 1 and 4 of Planck Collaboration (2020d). As known from previous analyses, the lensing bispectrum is detected at a value rather low but compatible with the expected amplitude of 1. As the detected value is extremely close to the *Planck* 2018 result, we recall that in Planck Collaboration (2020d) it was pointed out that performing the same analysis on maps where the Sunayev-Zeldovich (SZ) signal has been removed in addition to the galactic foreground contribution increases the measured lensing amplitude to a value much closer to 1. This is likely due to the correlations between the ISW and tSZ (thermal SZ) effects that produce another bispectrum, as was first shown by Hill (2018). These maps have not been produced for the PR4 release, which implies that we could not perform a similar analysis. However, it was verified by Jung et al. (2020) and Coulton et al. (2023) that the ISW-tSZ bispectrum amplitude is too small at the *Planck* resolution to

impact significantly our constraints on PNG and we expect the same conclusion to hold here.

The unclustered point sources and CIB amplitudes,  $b_{\text{PS}}$  and  $b_{\text{CIB}}$  respectively, are estimated jointly as these two shapes are highly correlated. The former is detected at a nearly  $3\sigma$  level in the data. However, it is important to recall that unlike the lensing bispectrum, this shape has a very low correlation with the various primordial templates, and therefore cannot contaminate the results presented in Table 1. The results for these two templates are only shown for temperature. The CIB is not expected to be polarized, and no polarized version of its template exists. As for unclustered point sources, none are detected in polarization, and as the point sources in temperature and polarization are not necessarily the same, it does not make sense to do a T+E analysis.

In Table 4, we illustrate the improvement in constraints achieved with the PR4 dataset compared to the PR3 results (using SEVEM for both). First, we show the expected refinement computed with a Fisher approach. This improvement ranges from a few up to a dozen percent, depending on the shape and if temperature and/or polarization is considered. In the most constraining case, which is the binned bispectrum T+E analysis, smaller error bars (by 7, 4 and 8% for the local, equilateral and orthogonal shapes, respectively, and 11% for lensing) are predicted. Second, we do the same comparison between error bars determined in the actual analyses using the binned bispectrum and integrated bispectrum estimators on the *Planck* PR4 and PR3 datasets. In most cases, they are very close to the Fisher forecast. For the binned bispectrum T+E analysis, the improvement is however slightly lower than expected for the local shape, and higher for the orthogonal and lensing shapes, with a difference of 4% each time. This small difference can be explained by the fact that the error bars themselves are determined with a relative error of 4.1% and 2.8% for PR3 and PR4,<sup>5</sup> respectively. Another important result to mention is that all estimator error bars are compatible with their Fisher predictions. Only for the lensing shape do we obtain results that are slightly suboptimal, with a smaller difference in the case of PR4 (15% in PR4 vs 21% in PR3 for the binned bispectrum T+E).

<sup>5</sup> The relative error on the standard deviation is given by  $1/\sqrt{2(n-1)}$  where  $n$  is the number of simulations used (300 and 600 for PR3 and PR4, respectively).

**Table 1.** Constraints on PNG from *Planck* PR4

Estimator	Independent			Lensing bias subtracted		
	Local	Equilateral	Orthogonal	Local	Equilateral	Orthogonal
<b>T</b>						
Binned	$8.9 \pm 5.5$	$23 \pm 72$	$-12 \pm 35$	$1.5 \pm 5.5$	$23 \pm 72$	$14 \pm 35$
Integrated	$11.5 \pm 7.3$	–	–	$7.2 \pm 7.3$	–	–
<b>E</b>						
Binned	$17 \pm 24$	$21 \pm 150$	$-31 \pm 77$	$16 \pm 24$	$20 \pm 150$	$-30 \pm 77$
<b>T + E</b>						
Binned	$4.9 \pm 5.0$	$8 \pm 46$	$-18 \pm 21$	$-0.1 \pm 5.0$	$6 \pm 46$	$-8 \pm 21$

**Notes.** The constraints on the PNG amplitude parameters  $f_{\text{NL}}^{\text{local}}$ ,  $f_{\text{NL}}^{\text{equil}}$  and  $f_{\text{NL}}^{\text{ortho}}$  are determined independently (Eq. 23) using the binned and integrated bispectrum estimators. Temperature and polarization maps produced by SEVEM from the PR4 dataset are used, including 600 simulations to evaluate error bars. Constraints are shown both for temperature and polarization independently, and jointly, and without and with taking into account the bias due to the lensing bispectrum.

**Table 2.** Joint constraints on NG from *Planck* PR4

Estimator	Local	Equilateral	Orthogonal	Lensing	Point sources/ $10^{29}$	CIB/ $10^{27}$
<b>T</b>						
Binned	$6.7 \pm 6.6$	$23 \pm 72$	$14 \pm 35$	$0.45 \pm 0.30$	$7.3 \pm 2.5$	$0.03 \pm 1.3$
Integrated	$7.2 \pm 8.2$	–	–	$1.01 \pm 1.06$	–	–
<b>E</b>						
Binned	$24 \pm 34$	$-33 \pm 166$	$5 \pm 105$	$-4.6 \pm 4.2$	–	–
<b>T + E</b>						
Binned	$0.5 \pm 6.2$	$3 \pm 49$	$13 \pm 25$	$0.62 \pm 0.23$	–	–

**Notes.** The constraints on the bispectrum amplitude parameters (both primordial and non-primordial) are determined jointly (Eq. 26) using the binned and integrated bispectrum estimators. Temperature and polarization maps produced by SEVEM from the PR4 dataset are used, including 600 simulations to evaluate error bars. Constraints are shown both for temperature and polarization independently, and jointly.

**Table 3.** Constraints on non-primordial NG from *Planck* PR4

Estimator	lensing	$b_{\text{PS}}/10^{-29}$	$b_{\text{CIB}}/10^{-27}$
<b>T</b>			
Binned	$0.53 \pm 0.29$	$6.9 \pm 2.5$	$0.2 \pm 1.3$
Integrated	$1.48 \pm 0.94$	–	–
<b>E</b>			
Binned	$-4.1 \pm 4.2$	–	–
<b>T + E</b>			
Binned	$0.64 \pm 0.23$	–	–

**Notes.** See Table 1 for more details. Note that the amplitudes of the unclustered point sources  $b_{\text{PS}}$  and CIB  $b_{\text{CIB}}$  bispectra are estimated jointly.

These different results confirm the tightening of the constraints on the NG amplitude parameters obtained from a bispectrum analysis of the *Planck* PR4 data. The few percent improvement for the primordial local, orthogonal, and equilateral constraints makes them the most stringent constraints on these parameters to date, without changing the main conclusions of

the previous *Planck* PNG analysis based on the PR3 data (Planck Collaboration 2020d).

## 6. Validation tests

To confirm the robustness of our data analysis results presented in Sect. 5, we apply the same pipelines to the *Planck* PR4 simulations. In Table 5, we show the amplitude parameters averaged over the 600 available simulations and their corresponding standard errors, for the primordial local, equilateral and orthogonal templates, and the lensing shape.

We verify that the PNG  $f_{\text{NL}}$ 's are consistent with the expected value of zero, as no PNG is included in the simulations. While there are small deviations from zero (of order 1 to  $1.5\sigma$ ) in the T or E-only analyses for the local and equilateral shapes, they disappear in the binned T+E case, which provides the most stringent constraints. The situation is similar for the orthogonal shape, which however has a slightly stronger deviation ( $2.5\sigma$ ) in the binned T-only analysis. Even if this would turn out not to be a statistical fluctuation, this deviation is still one order of magnitude smaller than the error bar on one map, used for the constraints in Table 1, and thus cannot bias our results in any significant manner.

**Table 4.** Error bar comparison between *Planck* PR3 and PR4

	Binned			Integrated
	$T$	$E$	$T + E$	$T$
<b>Fisher</b>				
Local	0.96	0.83	0.93	0.98
Equilateral	0.98	0.94	0.96	–
Orthogonal	0.92	0.88	0.92	–
Lensing	0.88	0.76	0.89	0.95
Point sources	0.88	–	–	–
CIB	0.91	–	–	–
<b>Observed</b>				
Local	0.96	0.81	0.97	0.94
Equilateral	1.03	0.95	0.96	–
Orthogonal	0.90	0.88	0.88	–
Lensing	0.88	0.69	0.85	0.89
Point sources	0.86	–	–	–
CIB	0.90	–	–	–

**Notes.** Ratio of the bispectrum amplitude parameter error bars (PR4 divided by PR3, using SEVEM for both) for the different shapes considered in Tables 1 and 3.

Concerning the lensing bispectrum, we find a significant deviation from the expected value of 1, with both estimators and in all cases (although the significance is lower for the binned E-only and integrated bispectrum analyses, due to much larger error bars). In the remainder of the section, we check several possible origins of this issue and verify that it has no impact on our observational constraints derived from the *Planck* PR4 data. However, we want to stress that even if this deviation is significant statistically due to the averages computed from many simulations, it still represents only a small fraction of the  $1\sigma$  observational error bars and is therefore negligible with respect to the statistical fluctuations expected in the data maps.

We have performed a series of tests to confirm that this issue is already present at the level of the original CMB simulations and thus is neither an artifact of the *Planck* PR4 NPIPE pipeline nor of the SEVEM component separation technique. First, we do a direct comparison of the *Planck* PR3 and PR4 simulation results. For both releases, lensed CMB realizations have been produced and processed through different pipelines to reproduce as accurately as possible the different instrumental effects (see Planck Collaboration (2020a,b,c) and Planck Collaboration (2020e) for details on PR3 and PR4, respectively). There is a common set of 100 CMB seeds fully processed for both releases (the ones numbered from 200 to 299).

In Table 6, we show the results obtained from the analysis of these 100 simulations for both PR3 and PR4 using the binned bispectrum estimator. Concerning the local, equilateral and orthogonal shapes, the measured  $f_{\text{NL}}$  values are compatible with the expected absence of PNG in these simulations. The lensing bispectrum is measured with similar amplitudes for the T and T+E amplitudes in both sets close to a value of 0.9, a few  $\sigma$  below the expected value of 1 (the E-polarization error bars are one order of magnitude larger and thus not sufficient to detect any deviation of the same order). This means that the new processing of instrumental effects used in the PR4 simulations does not bias

the lensing results, at least with respect to the PR3 results. Note that in this specific set of 100 simulations, most error bars are of the same order between the two releases. This is because 100 simulations are not sufficient to obtain fully converged numerical results that can show the small improvements obtained with PR4 that we highlighted in Sect. 5.

We also evaluate the impact of the cleaning technique SEVEM on the PNG results. We have to focus on the PR3 simulated maps, as more component separation methods were applied for that release. In Planck Collaboration (2020d), the main reported results were based on the method SMICA (Cardoso et al. 2008). In Table 7 we verify that on the 300 available PR3 simulations, we obtain very similar results. By comparison of Tables 6 and 7, we directly see that the results are extremely close to each other, at a level much better than the expected error bars. As the two cleaning procedures are based on very different methods, no correlation of possible biases is expected, and thus this confirms that neither the PNG nor the lensing bispectrum amplitudes are biased by SEVEM.

A further investigation of this small discrepancy between the measured lensing amplitude in the simulations and the expected value of 1 would require to check in detail steps like the lensing implementation in the CMB simulations based on LensPix (Lewis 2005) and the accuracy of the theoretical computation of the lensing bispectrum. This is however beyond the scope of this work and thus we focus here on confirming that this discrepancy does not have an impact on the reported observational constraints.

The binned and integrated bispectrum estimators explicitly reconstruct the bispectrum in addition to measuring amplitude parameters. This allows us to use the averaged bispectrum from the simulations as a theoretical template, to estimate how much it can bias the results from the observations. In Table 8, we show the  $f_{\text{NL}}$  parameters of the local, equilateral, and orthogonal shapes measured in the PR4 data, after subtracting the bias of the averaged simulation bispectrum. As can be verified by comparison to Table 1, these results are extremely close to the values obtained by removing the standard lensing theoretical bias, with deviations one order of magnitude smaller than the  $1\sigma$  error bars. This confirms that even if there is a small discrepancy between the simulations and the expected theoretical predictions, it is much too small to affect the reported observational constraints, at least as far as the central values are concerned.

We now check the impact on the error bars. We focus on the local PNG shape, which is by far the most correlated with the lensing bispectrum as they both peak in the squeezed limit. We use the integrated bispectrum estimator with subsets of 100 simulations taken among the 600 available ones to compute both the linear correction term and the error bars (for temperature alone). We randomly draw many of such subsets and measure the average lensing amplitude of the simulations, as well as the central value and error bar of  $f_{\text{NL}}^{\text{local}}$ . For all these sets, we show the corresponding values in Fig. 2. Although there is a variation of both  $f_{\text{NL}}^{\text{local}}$  and its error bar depending on the specific subset, the results confirm that it is uncorrelated to the lensing amplitude of the specific subset and that it is actually compatible with the differences expected from a random Gaussian field.

## 7. Conclusions

In this work we performed the first analysis of the standard non-Gaussian bispectrum templates on the *Planck* PR4 CMB data (Planck Collaboration 2020e), both temperature and E-polarization. These are the local, equilateral and orthogonal pri-

**Table 5.** Bispectrum amplitude parameters in the 600 *Planck* PR4 simulations

	Binned			Integrated
	$T$	$E$	$T + E$	$T$
Local	$-0.35 \pm 0.23$	$0.19 \pm 0.96$	$0.02 \pm 0.20$	$-0.21 \pm 0.30$
Equilateral	$3.2 \pm 2.9$	$-9.0 \pm 6.1$	$1.1 \pm 1.9$	–
Orthogonal	$3.4 \pm 1.4$	$-4.8 \pm 3.1$	$1.0 \pm 0.9$	–
Lensing	$0.925 \pm 0.012$	$0.71 \pm 0.17$	$0.939 \pm 0.009$	$0.90 \pm 0.04$

**Notes.** The amplitude parameters are determined with the same estimators as the data analyses presented in Sect. 5 from the 600 SEVEM PR4 simulations. We show the average values, and the corresponding standard errors. The lensing bias is subtracted from the three PNG shapes (local, equilateral and orthogonal).

**Table 6.** Bispectrum amplitude parameters in the 100 common *Planck* PR3 and PR4 simulations (SEVEM)

	PR3			PR4		
	$T$	$E$	$T + E$	$T$	$E$	$T + E$
Local	$-0.54 \pm 0.60$	$-3.6 \pm 3.1$	$-1.00 \pm 0.56$	$0.19 \pm 0.56$	$-4.5 \pm 2.4$	$0.39 \pm 0.52$
Equilateral	$2.7 \pm 7.1$	$-19 \pm 16$	$-0.9 \pm 4.5$	$0.7 \pm 7.2$	$-19 \pm 15$	$1.7 \pm 4.6$
Orthogonal	$-2.8 \pm 3.3$	$9.9 \pm 9.2$	$1.2 \pm 2.5$	$0.4 \pm 3.1$	$1.0 \pm 7.1$	$0.5 \pm 2.2$
Lensing	$0.898 \pm 0.030$	$1.37 \pm 0.65$	$0.907 \pm 0.025$	$0.893 \pm 0.032$	$0.66 \pm 0.41$	$0.927 \pm 0.025$

**Notes.** The amplitude parameters are determined with the binned bispectrum estimator from the 100 SEVEM PR3 and PR4 simulations that share the same CMB seeds. We show the average values, and the corresponding standard errors. The lensing bias is subtracted from the three PNG shapes (local, equilateral and orthogonal).

**Table 7.** Bispectrum amplitude parameters in the 300 *Planck* PR3 simulations with two different component separation techniques

	SEVEM			SMICA		
	$T$	$E$	$T + E$	$T$	$E$	$T + E$
Local	$0.09 \pm 0.33$	$-0.02 \pm 1.7$	$-0.70 \pm 0.30$	$0.06 \pm 0.32$	$0.01 \pm 1.5$	$-0.72 \pm 0.29$
Equilateral	$6.1 \pm 4.0$	$-9.9 \pm 9.1$	$0.4 \pm 2.8$	$5.6 \pm 4.0$	$-5.7 \pm 8.4$	$0.3 \pm 2.8$
Orthogonal	$-0.5 \pm 2.3$	$9.3 \pm 5.1$	$2.6 \pm 1.4$	$-0.1 \pm 2.3$	$7.1 \pm 4.8$	$2.9 \pm 1.4$
Lensing	$0.898 \pm 0.030$	$1.37 \pm 0.65$	$0.960 \pm 0.015$	$0.977 \pm 0.019$	$0.85 \pm 0.30$	$0.962 \pm 0.015$

**Notes.** The amplitude parameters are determined with the binned bispectrum estimator from the 300 SMICA and SEVEM PR3 simulations. We show the average values, and the corresponding standard errors. The lensing bias is subtracted from the three PNG shapes (local, equilateral and orthogonal).

primordial templates, and the secondary bispectrum templates for lensing, unclustered extra-galactic point sources and the CIB. The results of the full T+E analysis are  $f_{\text{NL}}^{\text{local}} = -0.1 \pm 5.0$ ,  $f_{\text{NL}}^{\text{equil}} = 6 \pm 46$  and  $f_{\text{NL}}^{\text{ortho}} = -8 \pm 21$ . While the improvements of the error bars are only a few percent with respect to the PR3 results (up to 12% for orthogonal), these now stand as the best constraints on primordial non-Gaussianity from *Planck*. As the error bars were determined from 600 simulations instead of 300 for PR3, they should also be even more accurate. Results are fully consistent with the PR3 results and no primordial non-Gaussianity is detected.

The analysis in this paper is necessarily more limited than the one in the full *Planck* collaboration paper on primordial non-Gaussianity for PR3 (Planck Collaboration 2020d). In the first place this is due to the available maps: only the SEVEM component separation technique was applied to the PR4 maps to pro-

duce everything needed for a non-Gaussianity analysis. For PR3 four different component separation techniques were applied, including SMICA that was chosen as the default method in all previous releases. In the second place this is due to using only one effectively optimal bispectrum estimator, the binned bispectrum estimator, with support from the non-optimal but very fast integrated bispectrum estimator for cross-checking certain results and running additional tests. For PR3 three different effectively optimal estimators (with four independent pipelines) were used, including the KSW estimator that was chosen as the default for the three primordial shapes in the previous releases. In fact we originally planned to have also results with the modal bispectrum estimator in this paper, but due to time constraints and computational resource limitations this was not possible in the end. However, it was shown in all previous releases that the results from the different component separation techniques and the different bispectrum estimators are fully consistent using many dozens of

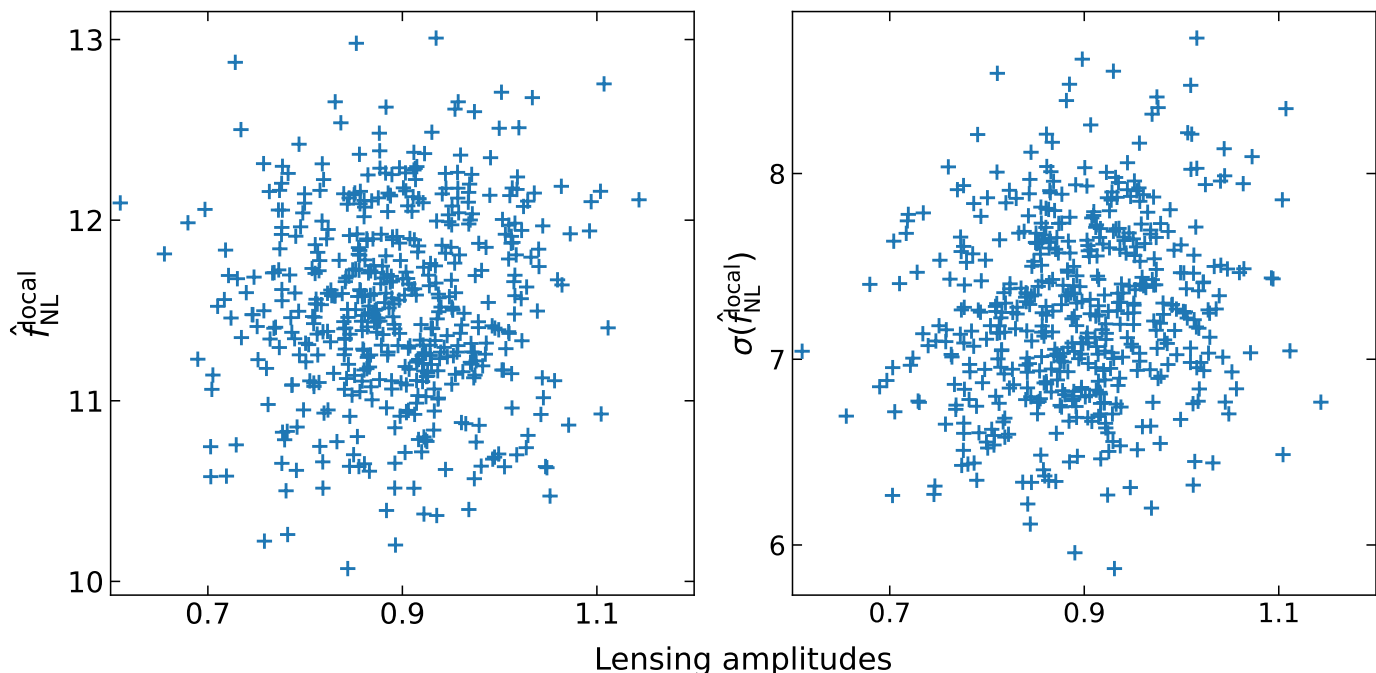


**Fig. 2.** Estimated  $\hat{f}_{\text{NL}}^{\text{local}}$  (left) and its error bar  $\sigma(\hat{f}_{\text{NL}}^{\text{local}})$  (right) using different subsets of the PR4 simulations for linear correction and error bars, as a function of the lensing amplitude in the corresponding subset, determined using the integrated bispectrum estimator. Each subset consists of 100 maps drawn randomly from the 600 SEVEM PR4 simulations. Note that the expected lensing bias of 4.3 on the estimated  $\hat{f}_{\text{NL}}^{\text{local}}$  has not been subtracted.

**Table 8.** Constraints on PNG from *Planck* PR4 with different bias subtraction

Estimator	Local	Equilateral	Orthogonal
		<b>T</b>	
Binned	$0.9 \pm 5.5$	$20 \pm 72$	$12 \pm 35$
Integrated	$7.4 \pm 7.3$	–	–
		<b>E</b>	
Binned	$16 \pm 24$	$23 \pm 150$	$-30 \pm 77$
		<b>T + E</b>	
Binned	$-0.6 \pm 5.0$	$5 \pm 46$	$-9 \pm 21$

**Notes.** Similar to the right-hand side of Table 1, but with a different lensing bias subtraction. Here the bias due to the averaged bispectrum of the 600 PR4 CMB SEVEM simulations has been subtracted from each reported PNG amplitude.

validation tests, and the binned bispectrum pipeline used here is the same as that used and fully validated in the past releases. In addition, as described we performed many validation tests for this paper as well. Hence the results should be fully robust.

Regarding the non-primordial templates, as in PR3 we detect lensing and unclustered point sources but no CIB (in a joint analysis of the latter two). Also similar to PR3, the measured lensing signal is a bit low compared to the expected value of 1, although compatible with 1 given the size of the error bars. It should be pointed out that in PR3 the variation between the four component separation techniques was larger regarding the non-primordial shapes, and SEVEM was the one with the highest point source signal and the lowest lensing signal. In the PR3 paper it was pointed out that the low lensing signal might be a

consequence of the correlation between the lensing template and another bispectrum describing the correlation between the ISW and tSZ effects. This was made plausible by showing that the lensing signal was much closer to unity in maps where the tSZ contribution had been removed, although no final conclusions could be drawn given the size of the error bars and the lack of significance. Lacking PR4 maps where the tSZ contribution has been removed, we could not redo this check here.

We performed several validation tests, the most interesting of which we report in this paper. In particular we checked that our pipeline works as expected on the 600 simulations. While we found no PNG in these simulations as expected, we were surprised to detect a very significant deviation downwards from 1 for the lensing shape. As the simulations contain no foregrounds, this cannot be due to the tSZ effect. Further investigation showed that this was not due to NPIPE, the new data-processing pipeline in PR4, nor to SEVEM, but was already present in the original CMB seed simulations for PR3 (that were reused in PR4). Due to a fortuitous choice of simulations for the PR3 analysis, this effect was not as notable at the time. However, we show that this mismatch of the lensing bispectrum in the simulations has no impact on our reported results for the CMB data map, neither regarding the central values nor the error bars.

PNG remains one of the most important sources of information about inflation and the early universe in general. Hence it is important to improve our constraints and their robustness, as we did in this paper, even if the improvement is modest. While undetected so far, that non-detection of PNG has already ruled out many models of inflation and alternatives. New observational data, from CMB or large-scale structure, whether they lead to a detection or a further tightening of the constraints, can only improve our knowledge of the early universe. PNG has the additional advantage that, unlike the tensor-to-scalar ratio, the prediction from single-field slow-roll inflation provides a clear

lower limit to  $f_{\text{NL}}$ . And while waiting for new experiments to come online and provide data, the wealth of information represented by the *Planck* data is here and, who knows, might still contain some surprises regarding as yet untested bispectrum templates. . .

*Acknowledgements.* We thank Michele Liguori for useful inputs and discussions. GJ and NA acknowledge support from the ANR LOCALIZATION project, grant ANR-21-CE31-0019 / 490702358 from the French Agence Nationale de la Recherche / DFG. This research made use of observations obtained with *Planck* (<http://www.esa.int/Planck>), an ESA science mission with instruments and contributions directly funded by ESA Member States, NASA, and Canada. The authors acknowledge the use of the *healpy* and *HEALPix* packages (Zonca et al. 2019; Górski et al. 2005). We gratefully acknowledge the IN2P3 Computer Centre (<https://cc.in2p3.fr>) for providing the computing resources and services needed for the analysis with the binned bispectrum estimator.

## References

- Achúcarro, A. et al. 2022 [arXiv:2203.08128]  
 Agullo, I., Bolliet, B., & Sreenath, V. 2018, *Phys. Rev. D*, 97, 066021  
 Allys, E. et al. 2023, *PTEP*, 2023, 042F01  
 Arkani-Hamed, N. & Maldacena, J. 2015 [arXiv:1503.08043]  
 Bartolo, N., Fasiello, M., Matarrese, S., & Riotto, A. 2010, *JCAP*, 08, 008  
 Bartolo, N., Komatsu, E., Matarrese, S., & Riotto, A. 2004, *Phys. Rept.*, 402, 103  
 Baumann, D. 2011, in *Theoretical Advanced Study Institute in Elementary Particle Physics: Physics of the Large and the Small*, 523–686  
 Bennett, C. L. et al. 2013, *Astrophys. J. Suppl.*, 208, 20  
 Bucher, M., Racine, B., & van Tent, B. 2016, *JCAP*, 05, 055  
 Bucher, M., Van Tent, B., & Carvalho, C. S. 2010, *MNRAS*, 407, 2193  
 Byrnes, C. T. & Choi, K.-Y. 2010, *Adv. Astron.*, 2010, 724525  
 Cabass, G., Ivanov, M. M., Philcox, O. H. E., Simonović, M., & Zaldarriaga, M. 2022a, *Phys. Rev. D*, 106, 043506  
 Cabass, G., Ivanov, M. M., Philcox, O. H. E., Simonović, M., & Zaldarriaga, M. 2022b, *Phys. Rev. Lett.*, 129, 021301  
 Cagliari, M. S., Barberi-Squarotti, M., Pardede, K., Castorina, E., & D’Amico, G. 2025 [arXiv:2502.14758]  
 Cardoso, J.-F., Martin, M., Delabrouille, J., Betoule, M., & Patanchon, G. 2008 [arXiv:0803.1814]  
 Chen, X. 2010, *Adv. Astron.*, 2010, 638979  
 Chen, X., Huang, M.-x., Kachru, S., & Shiu, G. 2007, *JCAP*, 01, 002  
 Chiang, C.-T., Wagner, C., Schmidt, F., & Komatsu, E. 2014, *JCAP*, 05, 048  
 Coulton, W., Miranthis, A., & Challinor, A. 2023, *Mon. Not. Roy. Astron. Soc.*, 523, 825  
 Coulton, W. R. & Spergel, D. N. 2019, *JCAP*, 10, 056  
 Creminelli, P., Nicolis, A., Senatore, L., Tegmark, M., & Zaldarriaga, M. 2006, *JCAP*, 05, 004  
 D’Amico, G., Lewandowski, M., Senatore, L., & Zhang, P. 2022 [arXiv:2201.11518]  
 de Putter, R., Gleyzes, J., & Doré, O. 2017, *Phys. Rev. D*, 95, 123507  
 Euclid Collaboration. 2011 [arXiv:1110.3193]  
 Fergusson, J. R. 2014, *Phys. Rev.*, D90, 043533  
 Fergusson, J. R., Liguori, M., & Shellard, E. P. S. 2010, *Phys. Rev.*, D82, 023502  
 Fergusson, J. R., Liguori, M., & Shellard, E. P. S. 2012, *JCAP*, 1212, 032  
 Fernandez-Cobos, R., Vielva, P., Barreiro, R. B., & Martínez-González, E. 2012, *Mon. Not. Roy. Astron. Soc.*, 420, 2162  
 Finelli, F. et al. 2018, *JCAP*, 04, 016  
 Gangui, A., Lucchin, F., Matarrese, S., & Mollerach, S. 1994, *Astrophys. J.*, 430, 447  
 Górski, K. M., Hivon, E., Banday, A. J., et al. 2005, *ApJ*, 622, 759  
 Gruetjen, H. F., Fergusson, J. R., Liguori, M., & Shellard, E. P. S. 2017, *Phys. Rev. D*, 95, 043532  
 Hill, J. C. 2018, *Phys. Rev. D*, 98, 083542  
 Hu, W. 2000, *Phys. Rev. D*, 62, 043007  
 Ivanov, M. M., Cuesta-Lazaro, C., Mishra-Sharma, S., Obuljen, A., & Toomey, M. W. 2024, *Phys. Rev. D*, 110, 063538  
 Jung, G., Oppizzi, F., Ravenni, A., & Liguori, M. 2020, *JCAP*, 06, 035  
 Jung, G., Racine, B., & van Tent, B. 2018, *JCAP*, 11, 047  
 Jung, G. & van Tent, B. 2017, *JCAP*, 05, 019  
 Karagiannis, D., Lazanu, A., Liguori, M., et al. 2018, *Mon. Not. Roy. Astron. Soc.*, 478, 1341  
 Komatsu, E. & Spergel, D. N. 2001, *Phys. Rev. D*, 63, 063002  
 Komatsu, E., Spergel, D. N., & Wandelt, B. D. 2005, *Astrophys. J.*, 634, 14  
 Komatsu, E. et al. 2011, *Astrophys. J. Suppl.*, 192, 18  
 Lacasa, F., Pénin, A., & Aghanim, N. 2014, *Mon. Not. Roy. Astron. Soc.*, 439, 123  
 Leach, S. M. et al. 2008, *Astron. Astrophys.*, 491, 597  
 Lehnert, J.-L. 2010, *Adv. Astron.*, 2010, 903907  
 Lewis, A. 2005, *Phys. Rev. D*, 71, 083008  
 Lewis, A., Challinor, A., & Hanson, D. 2011, *JCAP*, 03, 018  
 Maldacena, J. M. 2003, *JHEP*, 05, 013  
 Pénin, A., Lacasa, F., & Aghanim, N. 2014, *Mon. Not. Roy. Astron. Soc.*, 439, 143  
 Philcox, O. H. E. 2025 [arXiv:2502.06931]  
 Planck Collaboration. 2014, *Astron. Astrophys.*, 571, A24  
 Planck Collaboration. 2016, *Astron. Astrophys.*, 594, A17  
 Planck Collaboration. 2020a, *Astron. Astrophys.*, 641, A2  
 Planck Collaboration. 2020b, *Astron. Astrophys.*, 641, A3  
 Planck Collaboration. 2020c, *Astron. Astrophys.*, 641, A4  
 Planck Collaboration. 2020d, *Astron. Astrophys.*, 641, A9  
 Planck Collaboration. 2020e, *Astron. Astrophys.*, 643, A42  
 Renaux-Petel, S. 2015, *Comptes Rendus Physique*, 16, 969  
 Rigopoulos, G. I., Shellard, E. P. S., & van Tent, B. J. W. 2007, *Phys. Rev. D*, 76, 083512  
 Seery, D. & Lidsey, J. E. 2005, *JCAP*, 0506, 003  
 Senatore, L., Smith, K. M., & Zaldarriaga, M. 2010, *JCAP*, 01, 028  
 Tristram, M. et al. 2024, *Astron. Astrophys.*, 682, A37  
 van Tent, B., Delgado, P. C. M., & Durrer, R. 2023, *Phys. Rev. Lett.*, 130, 191002  
 Vernizzi, F. & Wands, D. 2006, *JCAP*, 05, 019  
 Wang, D.-G., Pimentel, G. L., & Achúcarro, A. 2023, *JCAP*, 05, 043  
 Wang, Y. 2014, *Commun. Theor. Phys.*, 62, 109  
 Yadav, A., Komatsu, E., Wandelt, B., et al. 2008, *Astrophys. J.*, 678, 578  
 Yadav, A. P. S., Komatsu, E., & Wandelt, B. D. 2007, *Astrophys. J.*, 664, 680  
 Zonca, A., Singer, L., Lenz, D., et al. 2019, *Journal of Open Source Software*, 4, 1298